SUPPLEMENTAL MATERIAL

This PDF file includes:

Supplementary Methods

Tables S1 to S4

Figs. S1 to S9

Supplemental Methods

Recordings of cellular action potentials in AF patients

Right atrial appendages were obtained from patients undergoing cardiac surgery. Experimental protocols were approved by the ethics committee of the University Medical Center Göttingen (No. 4/11/18), and informed consent was obtained from each patient. The patient samples were grouped in four blinded sets according to the diagnosis: Sinus Rhythm (SR), postoperstive AF (poAF), paroxysmal AF (pAF), and persistent AF (persAF). Episodes were classified as pAF if they terminate spontaneously within seven days, or persAF, if the episode lasted longer than one week.[70] Sinus rhythm patients were followed-up for 6 days to identify those with postoperative AF (poAF, any episode of AF lasting longer than 30 s) and without postoperative AF, classified as SR. Excised right atrial appendages were subjected to a standard protocol for myocyte isolation.[4] Right atrial myocytes were suspended in EGTA-free storage solution for subsequent simultaneous AP measurements.

Only rod-shaped myocytes with clear striations and defined margins were investigated. During experiments, myocytes were perfused with a bath solution at 37 °C containing (in mmol/L): $CaCl_2$ 2, glucose 10, HEPES 10, KCl 4, $MgCl_2$ 1, NaCl 140, probenecid 2; pH=7.35. The pipette solution contained (in mmol/L): EGTA 0.02, GTP-Tris 0.1, HEPES 10, K-aspartate 92, KCl 48, Mg-ATP 1, Na_2-ATP 4; pH=7.2. To evoke APs, 1 ms current pulses of 1.5–2 threshold strength were applied. The Pacing Cycle Length (PCL) was decreased in a stepwise manner, starting at 2064 ms and subsequently 1032, 516, 344, 258, 206, 172, 148, 129 ms. Pipette resistances in the range of 5–7 MΩ were utilized.

Due to computational limitations, a single patient from each group was chosen arbitrarily for model optimization (see below “Genetic algorithm”). Patients' data is given in **Table S1**, and APs restitution is shown in **Figure 1B, 4**. All patients were males undergoing coronary artery bypass surgery.

Acquisition of atrial anatomy in AF patients

Cardiac magnetic resonance imaging (MRI) was performed on a 1.5T scanner (Magnetom Avanto, Siemens Medical Systems, Erlangen, Germany) equipped with a 32-channel cardiac coil. LGE-MRI was performed 15 min after administering gadolinium chelates using a 3D, ECG-gated, respiratory-navigated, and inversion recovery-prepared Turbo Fast Low Angle

Shot sequence with fat saturation (voxel size: 1.25 × 1.25 × 2.5 mm^3). In the resulting images, the biatrial wall was manually contoured. Fibrotic and non-fibrotic tissue regions were differentiated using the image intensity ratio (IIR)-based approach[86]. The IIR of each atrial wall voxel was calculated by normalizing its LGE-MRI signal intensity to the mean intensity of the left atrial blood pool. Voxels with an IIR of >1.22 were classified as fibrotic; we have previously shown that regions with this property correlate to low-voltage areas observed during intracardiac mapping[86]. The IIR approach used here has been specifically designed to mitigate the uncertainty in threshold-based methods in segmenting LGE-MRI scans since it uses ratiometric values instead of raw voxel intensities[86]. Segmented images were up-sampled to an isotropic voxel size of 400 mm^3 using shape-based interpolation, and 3D finite element meshes were generated from the resulting high-resolution datasets using a previously developed approach. In each patient-derived model, myocardial fiber orientations were assigned using a rule-based method.[71]

Whole organ digital twin simulations

At the tissue level, conductivity values were assigned so that an effective longitudinal conduction velocity of 43.39 cm/s was achieved in the non-fibrotic myocardium, which was within the range of values recorded in patients with AF with 5:1 longitudinal\transverse anisotropy ratio, as previously.[14,72] Fibrotic regions were represented with remodeled electrophysiology, anisotropy, and conduction properties. The non-fibrotic action potential model was modified as described previously[15] to represent the regional electrophysiological changes due to fibrotic remodeling: 50% reduction in inward rectifier potassium current I_{K1}; 50% reduction in L-type calcium current I_{CaL}; and 40% reduction in sodium current I_{Na}. Conductivity values in fibrotic regions were reduced by 30% to represent decreased intercellular coupling due to replacement fibrosis, collagen deposition (interstitial fibrosis), and gap junction remodeling. Since fibrosis results in greater conduction velocity impairment in the direction transverse to cardiac fibers, the conductivity values were further modified to achieve a longitudinal to transverse anisotropy ratio of 8:1.[14]

Electrical wave propagation was governed by the monodomain formulation, and finite-element simulations were executed with the CARP software package.[73] As in previous study[14], in each patient-derived model, 40 pacing sites were distributed uniformly throughout the atria. For each pacing site, we ran a simulation that involved applying — at

the specified location — a clinically relevant pacing sequence of 12 electrical stimuli of 100 μA/cm3 with cycle lengths decreasing from 300 to 150 ms, to induce arrhythmias and thus assess the arrhythmogenic propensity of the fibrotic substrate. The whole pacing sequence lasted for 2.5 s, RD dynamics was simulated for 5 s after the end of the pacing. For each of the patient-derived models, we simulated 40 AF induction protocols, 1 for each pacing site.[14,15]

RNA-seq

Right atrial appendages were obtained from patients undergoing cardiac surgery. Tissues were immediately flash frozen in liquid nitrogen and stored at -80 °C. Total mRNA was extracted from approximately 40 mg of tissue with RNeasy Fibrous Tissue Mini Kit (Qiagen). RNA purity and yield were quality checked with Agilent Bioanalyzer to satisfy RIN >7 and total RNA amount 3-5 μg. The library was prepared using the TruSeq RNA Library Prep Kit (Illumina), and sequencing was performed on the Illumina HiSeq 2500, generating 30-40 million paired-end reads of 150 base pairs per sample. Sequence reads underwent trimming with Trimmomatic v0.36[74] to eliminate potential adapter sequences and low-quality nucleotides. The trimmed reads were then aligned to the Homo sapiens GRCh38 reference genome from ENSEMBL[75] using the STAR aligner v2.5.2b[76]. Unique gene hit counts were determined using featureCounts[77] from the Subread package v1.5.2[78], and the results were summarized and reported based on the gene_id feature in the annotation file. Only unique reads that mapped within exon regions were included in the counts. A one-way analysis of variance (ANOVA) followed by Tukey's Honest Significant Difference (HSD) test for multiple comparisons was used to determine statistical differences across groups, with a significance level set at $p < 0.05$.

The data discussed in this publication have been deposited in NCBI's Gene Expression Omnibus[79] and are accessible through GEO Series accession number GSE269882 (https://www.ncbi.nlm.nih.gov/geo/query/acc.cgi?acc=GSE269882).

Genetic algorithms

Maleckar AP model[80] was used in the study with the following modifications. Ventricular I_{CaL} current (I_{CaLv}) was added to the original Maleckar model as described in our preliminary study [81] in order to replicate phenotypic variability among AF patients as observed in

experimental AP recordings. The expression of the ventricular isoform of L-type calcium channel in AF is supported by RNA-seq studies[40] and our recent CAGE study.[39] I_{CaLv} was simulated as the modification of the I_{CaL} current in the O'Hara-Rudy model[82] modified by Tomek.[83] AP model is integrated using LSODA solver.[84] Relative and absolute tolerances were set as 10^{-4} and 10^{-7}, respectively.

AP model parameters were personalized to conform to the patch-clamp recordings *via* custom Genetic Algorithm modification.[35] Briefly, an initial generation of the organisms (different model parameter sets) is iteratively updated via selection, mutation, and crossover genetic operators to minimize the deviation between simulated and experimental AP waveform restitution. As described previously, only steady-state AP waveforms were considered the "proper" solution to the optimization problem. This was achieved by the inclusion of intracellular concentrations in the set of optimized parameters. A logarithmic scale was used for ionic channel conductivities during the optimization process. Optimized model parameters and AP markers for the model and experiment are in **Table S2.**

The parameter values were fitted via GA as in (40). In the current study, we used 1000 generations, 8192 organisms, and 128 elites. The following concentrations were set to the fixed experimental levels: $[Mg2+]_i$ 1 mM, $[Na+]_o$ 140 mM, $[Ca2+]_o$ 2 mM, $[K+]_o$ 4 mM. The following parameters were subjected to genetic operators: conductivities of INa, atrial and ventricular phenotypes of I_{CaL}, I_{to}, I_{Kur}, I_{K1}, I_{Kr}, I_{Ks}, I_{BNa}, I_{BCa}, I_{NaK}, I_{CaP}, I_{NCX}, RyR, SERCA and $[Na+]_i$, $[K+]_i$, $[Ca2+]_{rel}$ concentrations. Ionic current conductivity bounds were set from 0.1 to 10 times the original model value, except for INa (0.8, 10.0) and ICaL (0.01, 10.0). $[Na+]_i$ was mutated from 4 to 16 mM, $[K+]_i$ from 100 to 160 mM, $[Ca2+]_{rel}$ from 0.06 to 6.0 mM.

The following CLs were used: 2064, 1032, 516, 344 ms for persAF, poAF, SR; 516, 344, 256, 206 for the pAF. Longer periods for pAF trace were excluded due to experimental artifacts in the corresponding recordings.

The code of the GA can be found at https://github.com/humanphysiologylab/ga-meta .

Although output parameters were precise enough to observe pathology-specific differences in most import ionic currents: INa, ICaL, IK1 and Ito (**Figure 4**, main text), it was much less precise than in our previous study[35]. For example, in case if persAF standard deviation IK1 conductivity was 50% of the original Maleckar model value. Given that AP waveform is well-reproduced by all of these parameter sets, the imprecision does not affect the 3D simulations of non-fibrotic tissue. However, since fibrosis was simulated by relative changes

in IK1, ICaL and INa conductivities, parameters uncertainty affects AP waveform in the fibrotic tissue. The issue is illustrated in **Figure S1**. Each of the 10 GA optimization runs reproduce precise AP waveform in normal tissue (**Figure S1A**), but there is notable difference in resulting AP waveform in fibrotic tissue (**Figure S1B**). Most importantly the parameters uncertainty, in particular IK1 conductivity, affect the resting potential (RP) at larger PCLs (**Figures S1C,S1D**): the initial phase of repolarization is not affected by the uncertainty, while RP tends to converge to similar values at lower PCLs relevant to reentry simulations. This is explained by IK1 reduction by 50% in fibrosis model, which implies that larger IK1 conductivity in non-fibrotic model would result in larger depolarisation in fibrosis. Previously, it was shown that neonatal rat monolayers depolarize by 20% when compared to control myocytes at 2 Hz PCL[85]. Extreme changes of RP in a number of persAF models shown in **Figures S1B,C** could thus considered to be unphysiological. The set of parameters that we used in 3D simulations was chosen on the basis of minimal RMSE among several optimization runs, but as demonstrated in **Figure S1D** (black stars) all of these parameter sets resulted in RP depolarisation below 20 % in fibrotic tissue.

Backtracking algorithm

The algorithm consists of the following stages (Figure 2, main text).

1. We calculate the distance (h) and activation time delay (Δt) between neighboring vertices. For every activated vertex, we define the wavebreak as the event when $h/\Delta t < 1$ cm/s between any neighboring vertices. Such wavebreaks are depicted as white dots in Figure 2A. The threshold value of 1 cm/s implies that given the mesh element size of ~0.5 mm, the whole volume immediately surrounding the vertex was activated within 50 ms. It should be noted that dynamic wavebreak regions corresponding to RD with a rotation period of ~50 ms might be undetected by using this threshold, however we did not observe such short rotation periods in our simulations. Another extreme is slow conduction velocity that would be recognized as a wavebreak by the algorithm, but we did not observe CV<1 cm/s.
2. Two wavebreaks are ascribed to the same connected component if these were close in space and happened almost simultaneously, more precisely: $hwb/\Delta twb > 1$ cm/s. Three connected components are exemplified in Figure 2B by different colors.

3. For every component, we find the last activated vertex (colored circles in Figure 2C). The algorithm builds a trajectory by backtracking the velocity field (colored curves in Figure 2C). Since the core of the vortex29 is identified as a wavebreak on step 1, every reentrant driver can be located as a part of the trajectory starting from the corresponding core (Figure 3A). The conduction velocity was calculated as the inverse gradient of activation time: $\vec{CV} = \frac{\vec{\Delta t}}{|\vec{\Delta t}|^2}$.
4. The trajectories from step 3 should be segmented in two parts: quasiperiodic rotating source of excitation (solid colored line in Figure 2D), and the 'tail' connecting it with the wavebreak component. This is done via the neural network trained on synthetic trajectories (see Figure S2). We have used a modified U-Net to solve the segmentation problem.30 Neural network architecture is shown in Figure S3.

The complete pipeline is shown in Figure 2E. Note, that both RDs (blue, pink) and focal source of activation (stimulus) are detected by the BTA.

Wavebreak probability, P(wb)

For every vertex in the mesh, we calculate wavebreak probability as a proportion of the stimuli resulting in wavebreaks. Only the first 2.5 s of the simulations were considered for the probability estimate, that is, when the tissue was stimulated by a virtual pacing electrode and not by reentrant activity. To account for non-local properties of the fibrotic tissue, we calculated mean $P(wb) = \sum(\frac{v}{V}\frac{N_{wb}}{N_{stim}})$ as a weighted sum of the fractions, $\frac{N_{wb}}{N_{stim}}$, over the tetrahedrons constituting the volume. N_{wb} is the total number of the wavebreaks, N_{stim} is the total number of stimuli (480). The latter equals the number of simulations (40) times the number of stimuli per simulation (12). Weight, $\frac{v}{V}$ is the tetrahedron volume fraction. In order to calculate P(wb) within reentry drivers (**Figure 7, S10**) the following algorithm was used: (1) A deformed toroidal region was defined as part of scroll wave by labelling all vertices within 5 mm of 1D RD trajectory; (2) In all cases the torus was thicker than atrial wall essentially splitting the tissue in two components: the inner arrhythmogenic

region (tissue enclosed within the “hole“ of the torus and the scroll wave itself), and the outer non-arrhythmogenic region (remaining vertices).

CV calculation

We calculate velocity, CV, for the current tetrahedron given the activation times, $\vec{t} = \{t_1, t_2, t_3, t_4\}$, of the vertices and their coordinates, $X = \{\vec{x}_1, \vec{x}_2, \vec{x}_3, \vec{x}_4\}$.

$\vec{dx}_i = \vec{x}_i - \vec{x}_4$

U – 3x3 matrix, corresponding to the projection operator on the tetrahedron edges:

$U = \{\frac{\vec{dx}_1}{|\vec{dx}_1|}; \frac{\vec{dx}_2}{|\vec{dx}_2|}; \frac{\vec{dx}_2}{|\vec{dx}_2|}\}$.

$\vec{dt} = \{t_i - t_4\} = \{dt_1, dt_2, dt_3\}$

$\vec{\nabla t}_{proj} = \{\frac{dt_1}{|\vec{dx}_1|}, \frac{dt_2}{|\vec{dx}_2|}, \frac{dt_3}{|\vec{dx}_3|}\}$,

where $\vec{\nabla t}_{proj}$ – projections of the $\vec{\nabla} t$ onto tetrahedron edges; $\vec{\nabla} = \{\frac{\partial}{\partial x}, \frac{\partial}{\partial y}, \frac{\partial}{\partial z}\}$.

Then activation time gradient $\vec{\nabla} t$ is the solution of $U \cdot \vec{\nabla} t = \vec{\nabla t}_{proj}$.

The conduction velocity can then be calculated as the inverse gradient of activation time:

$\vec{CV} = \frac{\vec{\nabla} t}{|\vec{\nabla} t|^2}$

The code can be found at https://github.com/humanphysiologylab/heart-meshes/blob/1e94c4c71bdd7f2910d8798056e81426044251ac/src/mesh-free/calculate_cv.jl .

Synthetic trajectories.

Neural network was trained via a supervised learning algorithm. Since manual markup is tedious, we created a synthetic dataset that was marked up automatically (upon generation). Synthetic trajectories combined two regimes: rotor (quasi-periodic behavior) and non-rotor (non-periodic curve). Rotor segments of trajectory were modeled as a modulated combination of harmonic signals:

$$r(t) = S(t) \cdot \left[A_0 + A \cdot \sum_k sin(\omega_k t + \varphi_k)\right]$$

$S(t) \sim const + \alpha \cdot exp(-t/\tau)$ (squeezing)

$x(t) = r(t) \cdot cos(t)$

$y(t) = r(t) \cdot sin(t)$

Non-rotor segments were modeled as a random walk with the following smoothing via the moving average

$x_i = \sum_{k=0}^{i} \xi$, where $\xi \in U_{[-1, 1]}$

$\bar{x}_i = \frac{1}{n} \sum_{k=i-n+1}^{i} x_k$, window size $n = 50$.

All parameters were set manually to produce trajectories similar to the experimental ones. To generate the final trajectory, we concatenated rotor and non-rotor segments as follows: rotor → non-rotor → rotor → non-rotor, etc. New segment was added to the trajectory after translation and rotation in order to make the connection smooth (**Figure S2 A,B)**.
The code can be found at
https://github.com/humanphysiologylab/nn-rotor/blob/master/notebooks/001-Synthetic-rotors.ipynb .

Trajectory segmentation.

The straightforward approach to the trajectory segmentation is using $\vec{r}(t)$ as input to the neural network. However, this results in a number of undesirable artifacts: for example, a single misclassified pixel might split the reentrant driver (RD) in two, and consequently, the number of artifact RDs is increased dramatically, while their lifetime is reduced. Instead of that we used the matrix of pairwise euclidean distances between the trajectory points was used as input to neural network, *i.e.* $A(t_1, t_2) = ||\vec{r}(t_1) - \vec{r}(t_2)||_{L2}$ (**Figure S2 C,D**). The output matrix elements were supposed to be ***1*** if both $r(t_1)$ and $r(t_2)$ belong to the RD segment and ***0*** otherwise. Finally, each minimal diagonal block of the output matrix was interpreted as corresponding to a *single* reentrant driver if it contained a *single* connected component of non-zero elements***.*** This 2D matrix representation is very robust: as shown in **Figure S4** even **35** % of misclassified matrix elements result in correct trajectory segmentation. Segmentation of synthetic datasets (**Table S3**) resulted in 95% accuracy and 93% IoU (intersection over union). Segmentation of an actual BTA trajectory recovered from whole atria simulations and its 2D matrix representation is exemplified in **Figure S5**.

The following algorithm was used for the trajectory segmentation using its 2D representation (**Figure S4**):

(1) Fix some time i and duration n.

(2) Calculate the mean number of pixels classified as RDs, p, over the edge of the $n \times n$ square with a center at the diagonal $(i;\ i)$.

(3) If p is greater than a threshold (we set 0.75) then mark trajectory segment from $i - n/2$ to $i + n/2$ as a RD.

(4) Iterating over all possible i-s and n-s, we merge all RD segments with nonzero intersection.

Neural network architecture.

We have adapted the U-net model[30] (**Figure S3**). The network consists of two mirrored cascades: the downsampler and the upsampler. The downsampler iteratively halves spatial resolution (via max-pooling layers) and doubles the number of channels. The upsampler does the opposite job, doubles spatial resolution (via upsampling layer) and halves the number of channels. Both parts share the same core block which is a twice-repeated sequence of the following layers: convolutional (3x3 kernel), batch-normalization, and activation (ReLU). There are residual connections between the downsampler and upsampler. The network's input is a gray-scale square image while the output is a matrix of the same size, matrix elements are probabilities of the target class in the same position in the input image.

$$Loss(\widehat{y},\ y)\ =\ \beta \cdot BCELoss(\widehat{y},\ y)\ +\ (1\ -\ \beta) \cdot DiceLoss(\widehat{y},\ y),$$

where $\widehat{y}$ and y are predicted and true probabilities. Such loss function is also known as "ComboLoss".

$$BCELoss(\widehat{y},\ y)\ = -\sum \overline{y} \cdot log(\widehat{y})\ +\ (1\ -\ \overline{y}) \cdot log(1\ -\ \widehat{y})$$

BCELoss is Binary Cross Entropy Loss (for numerical stability, we used BCE with logits). Label smoothing was used for the true labels in BCELoss:

$$\overline{y}\ =\ (1\ -\ \alpha) \cdot y\ +\ \alpha \cdot ½$$

$$DiceLoss(\widehat{y},\ y)\ =\ \frac{2\cdot\sum\widehat{y}\cdot y}{\sum\widehat{y}+\sum y}$$

We used the following hyperparameters for loss function: $\alpha\ =\ 0.1,\ \beta\ =\ 0.5$.

The code can be found at https://github.com/humanphysiologylab/nn-rotor .

BTA comparison to Hilbert Transform.

In order to compare new BTA with the traditional Hilbert Transform PS algorithm we have simulated the reentry in 2D square tissue, 5 x 5 cm. Simulation lasted 1 s. The tissue was discretized in a rectangular grid with a 100 um step that resulted in 500 x 500 nodes. Transmembrane voltage was recorded at every 1 ms. SR AP model was used for all nodes. Both algorithms were implemented in the Julia programming language without multiprocessing.

Table S1. Patients' information.

	SR	poAF	pAF	persAF
Sex	male	male	male	male
Age, y	72	59	62	77
Body mass index, kg/m^2	26	27	41	23
CAD	Y	Y	Y	Y
MVD/AVD	N	N	N	N
Hypertension	Y	N	Y	Y
Diabetes	Y	N	N	N
Hyperlipidemia	N	N	Y	Y
LVEF,%	64	32	35	45
Digitalis	N	N	N	N
ACE inhibitors	N	N	Y	N
AT1 blockers	Y	N	N	N
b-Blockers	Y	N	Y	Y
Dihydropyridines	Y	N	N	N
Diuretics	Y	N	Y	N
Nitrates	N	N	N	N
Lipid-lowering drugs	Y	N	Y	Y

ACE, angiotensin-converting enzyme; AT, angiotensin receptor; ; BMI, body mass index; CAD, coronary artery disease; LVEF, left ventricular ejection fraction; MVD/AVD, mitral/aortic valve disease.

Table S2. AP Models' parameters. Conductivities scalers.

	persAF	pAF	poAF	SR
P_Na	0.82	0.80	0.80	1.18
g_Ca_L (Maleckar)	0.15	0.01	0.01	0.61
g_Ca_L (Tomek)	0.92	0.30	0.01	0.55
g_to	0.14	0.20	0.79	1.21
g_kur	0.12	0.56	0.10	0.10
g_K1	0.75	0.17	0.41	0.19
g_Kr	2.29	4.35	2.09	2.62
g_Ks	5.59	5.17	0.58	7.32
g_b_Na	2.74	0.18	0.66	0.22
g_b_Ca	0.54	0.26	0.11	0.11
i_NaK_max	0.35	0.28	0.28	0.61
i_CaP_max	9.49	1.24	0.17	0.13
K_NaCa	1.18	0.15	0.36	0.13
alpha_rel (RyR)	0.10	0.11	0.25	0.13
I_up_max (SERCA)	1.58	9.63	0.89	9.80

Table S3. Segmentation metrics for the synthetic dataset.
Mean, standard deviation, 25%, 50%, 75% quantiles are calculated for accuracy, IoU (Intersection over Union), segment offset, and onset.

	Train (n = 474)				Train (n = 117)			
	IoU, %	Offset, ms	Onset, ms	Accuracy, %	IoU, %	Offset, ms	Onset, ms	Accuracy, %
mean	93	58	-38	95	93	45	-40	95
std	8	238	77	5	6	181	58	5
25%	91	0	-6	93	91	0	-60	95
50%	95	20	-2	96	95	20	-20	97
75%	97	60	0	98	97	50	0	98

Table S4. AP markers, experiment vs model.

		APD80		Resting potential		AP Amplitude	
	CL	experim	model	experim	model	experim	model
persAF	344	65	64	-75.68	-75.39	118.71	112.46
	516	69	70	-77.82	-77.22	118.71	115.88
	1032	74	76	-79.80	-80.12	121.92	119.69
	2064	81	81	-81.18	-78.79	123.90	119.16
pAF	206	75	78	-71.72	-71.61	104.68	103.05
	258	81	83	-75.84	-75.01	113.37	110.35
	344	93	89	-76.14	-74.96	116.42	113.58
	516	92	101	-81.63	-82.35	127.11	123.40
poAF	344	95	92	-78.28	-76.55	107.27	111.54
	516	103	109	-79.50	-79.47	116.73	117.17
	1032	132	136	-81.63	-81.23	124.05	120.85
	2064	143	153	-82.09	-81.93	124.21	122.55
SR	344	125	114	-82.40	-78.45	133.06	123.08
	516	147	143	-82.40	-80.25	133.36	128.75
	1032	187	199	-87.13	-86.43	142.97	137.83
	2064	221	220	-85.45	-82.84	141.60	137.00

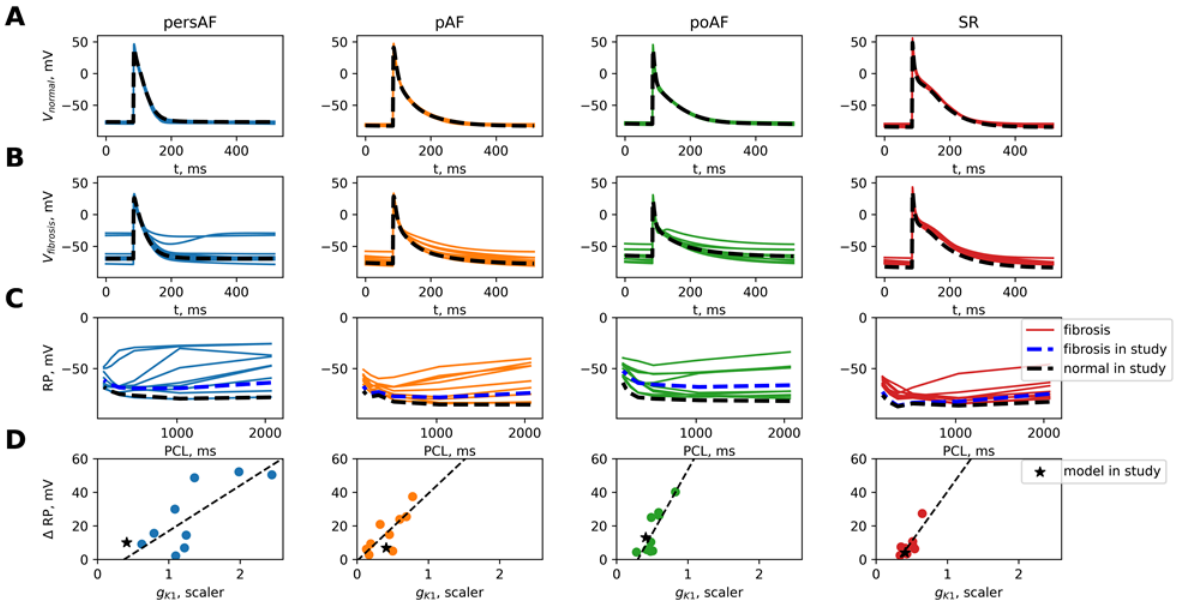

Figure S1. Parameters uncertainty effect on model predictions.
A. Normal atrial tissue, 10 GA runs reproduce the patch clamp experimental data. The model used in study shown by dashed black line.
B. Fibrotic tissue. Parameter uncertainty results in the discrepancy between the models in fibrosis. However, these models are different mostly in terms of the resting potential.
C. Resting potential restitution of the models in fibrosis (coloured lines) compared to model used in the study for normal tissue (black dashed line) and fibrosis (blue dashed line).
D. The RP differences at 1000 ms PCL are explained by IK1 conductivity. Since gK1 was reduced by 50% in fibrosis, large gK1 values resulted in unphysiologically depolarised RP. The pearson correlation coefficients are 0.76, 0.81, 0.84 and 0.79 for persAF, pAF, poAF and SR correspondingly.

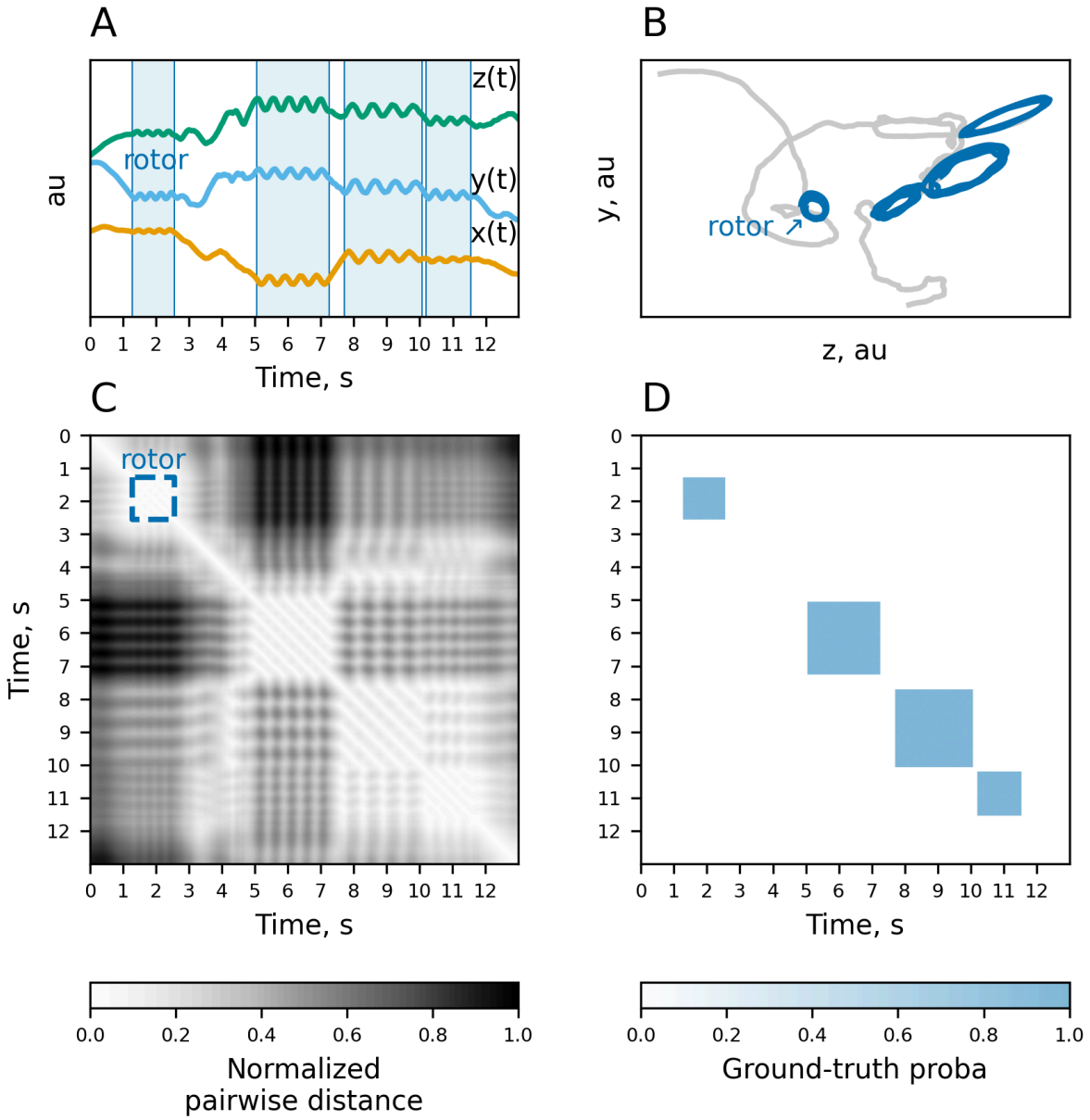

Figure S2. Example of the synthetic trajectory.

A. Trajectory coordinates. Blue shaded regions correspond to rotor segments.

B. Trajectory projection onto zy plane. Dark-blue and light-grey parts are rotor and non-rotor segments, respectively.

C. Normalized pairwise distances (euclidean) between trajectory points. This matrix is used as input for the neural network.

D. Ground-truth probability of the rotor (P). If i^{th} and j^{th} trajectory points belong to the same rotor segment then $P[i, j]$ and $P[j, i]$ are supposed to be equal to 1 (0, otherwise).

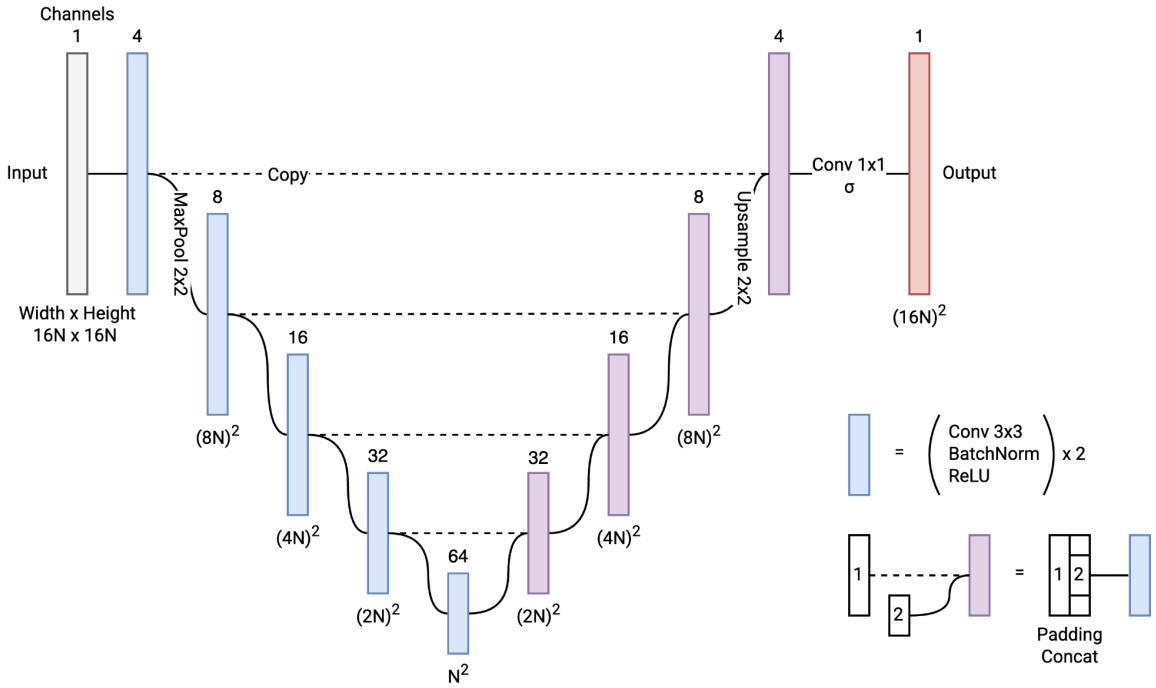

Figure S3. Neural network architecture.

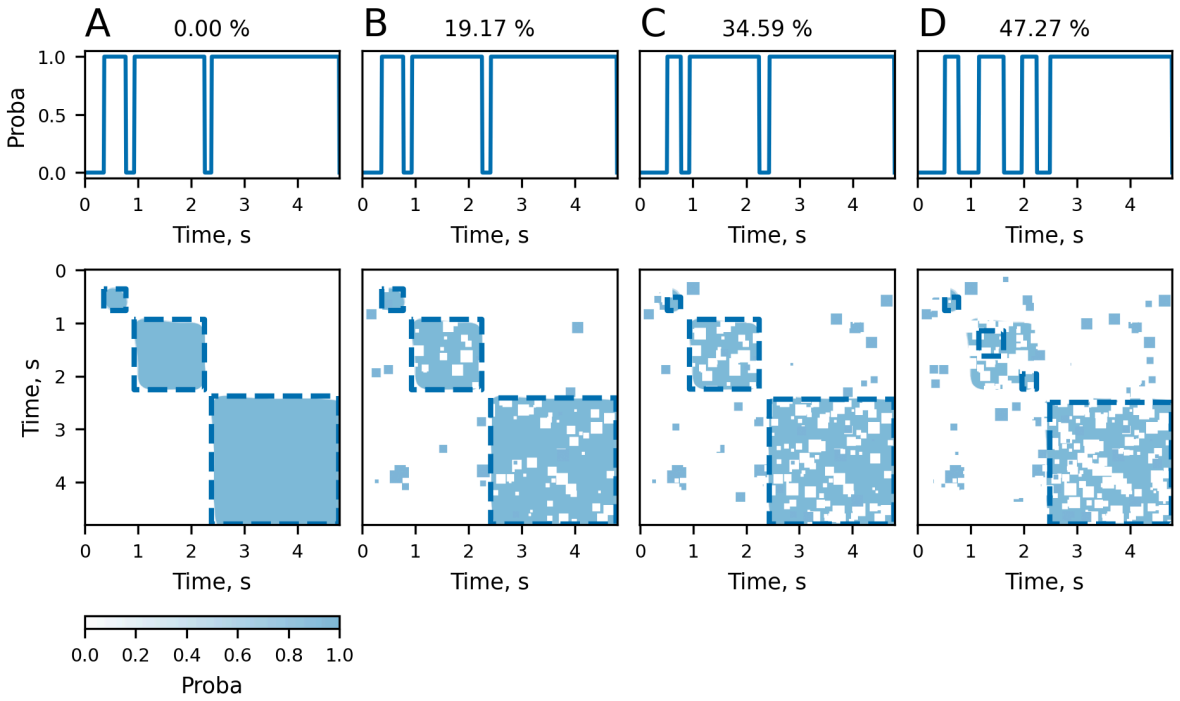

Figure S4. Segmentation of 2D matrices is robust.
Panels A-D correspond to the progressive increase in the misclassification rate (% of the misclassified pixels given in the subtitle). Even with 35% of the misclassified pixels, three reentrant driver segments were identified correctly.

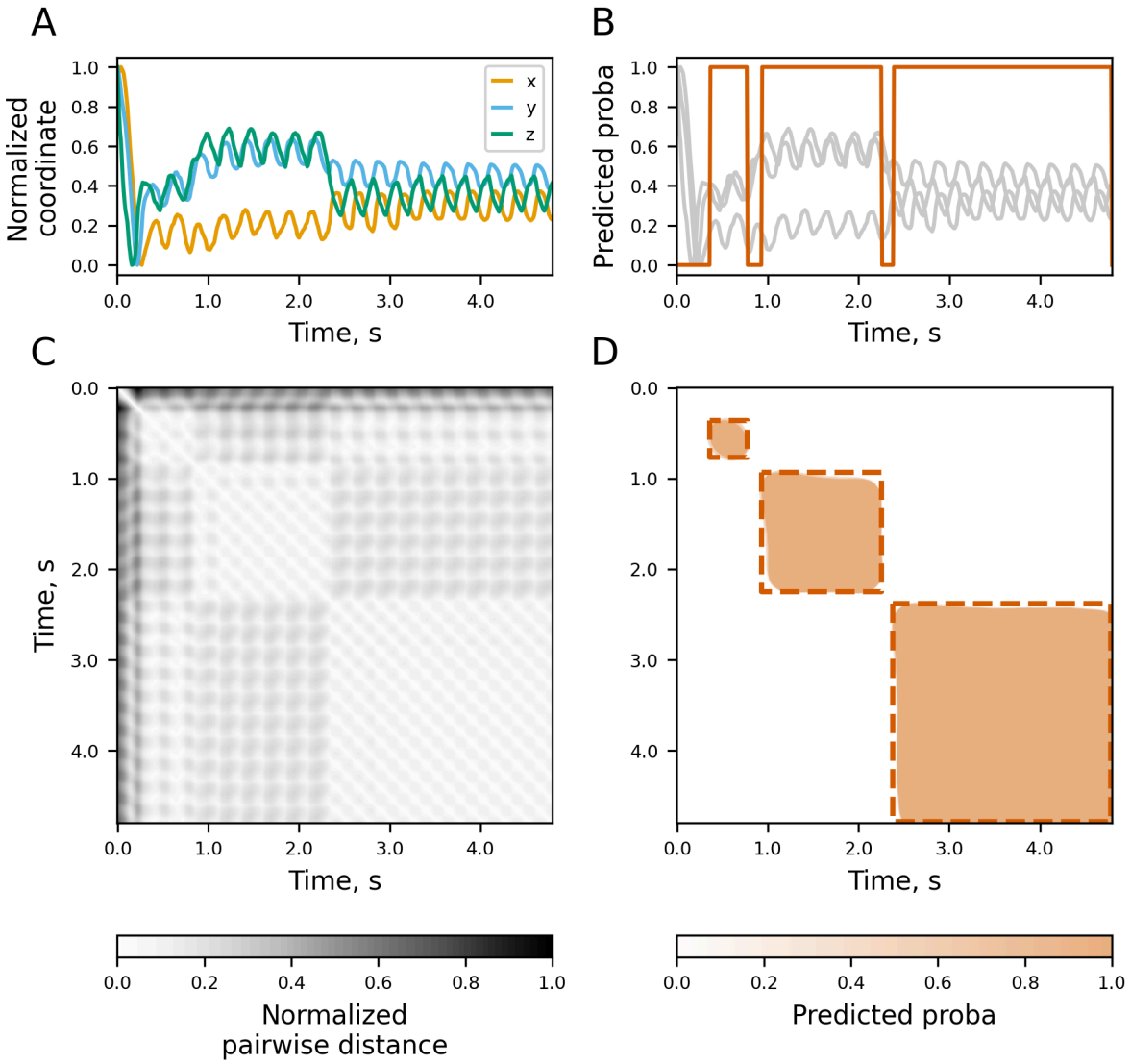

Figure S5. Example of the segmentation of the actual trajectory from the whole-atria simulations.

A. Trajectory coordinates.

B. Predicted probability (orange) of trajectory segment corresponding to reentrant driver.

C. Pairwise normalized distance (euclidean) between trajectory points. This matrix is used as an input to the convolutional neural network.

D. Predicted probability of the reentrant activity for the input 2D matrix. Three square-like orange blocks were classified as corresponding to reentrant drivers, dashed square section is used for final segmentation shown in (B).

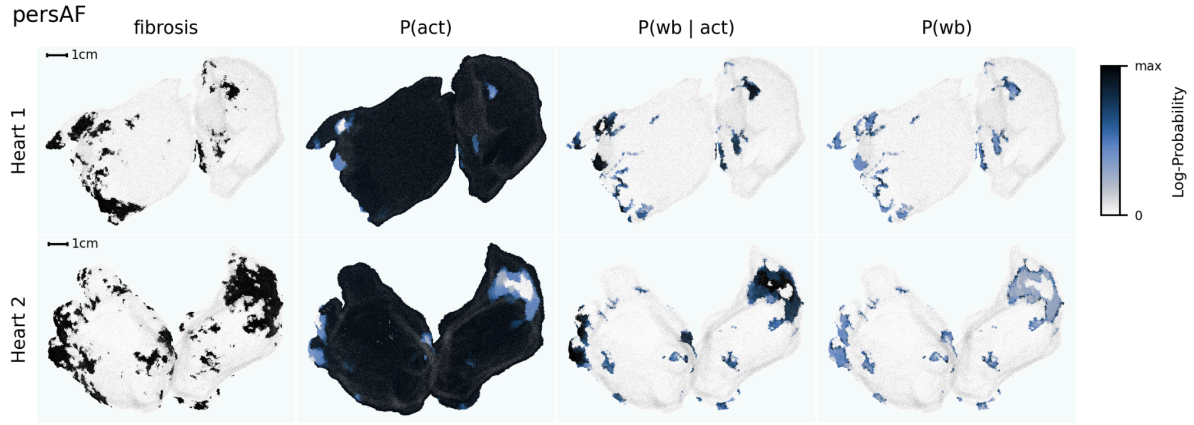

Figure S6. Example of activation/wavebreak probabilities for the persAF.
The first column corresponds to the fibrosis distribution (white and black are normal and fibrotic regions, respectively). The following columns from left to right are activation probability $P(act) = \frac{N(act)}{N(stimuli)}$, conditional wavebreak probability given the activation $P(wb \mid act) = \frac{N(wavebreaks)}{N(act)}$, unconditional wavebreak probability $P(wb) = P(wb \mid act) \cdot P(act) = \frac{N(wavebreaks)}{N(stimuli)}$. These probabilities were calculated over the first *2.5 s* of the simulation when the tissue was activated by pacing (not by arrhythmogenic reentrant drivers).

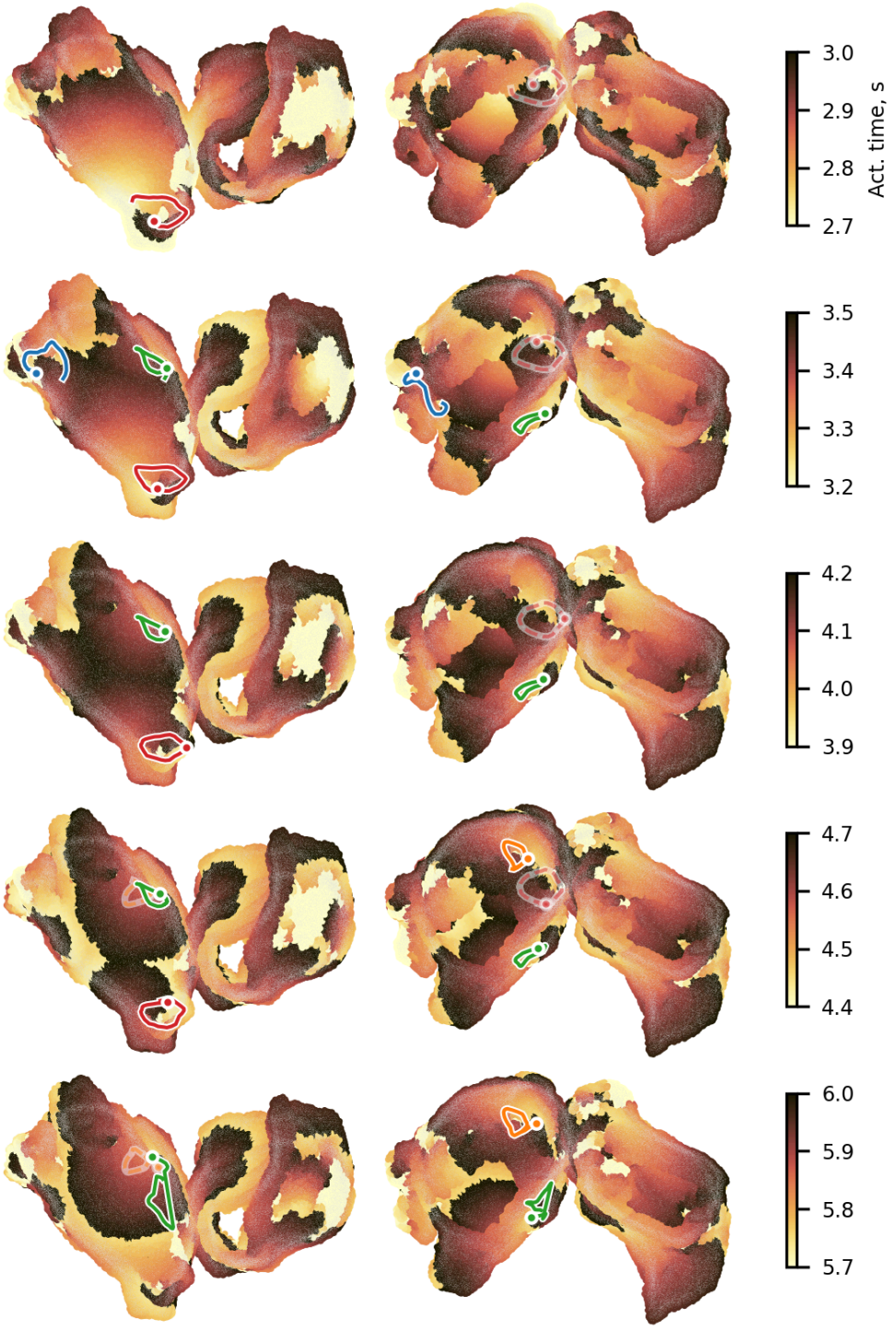

Figure S7. Activation sequence.
Representative evolution of propagation pattern. Arrhythmogenic pattern is driven by several simultaneous reentrant drivers shown by colored curves.

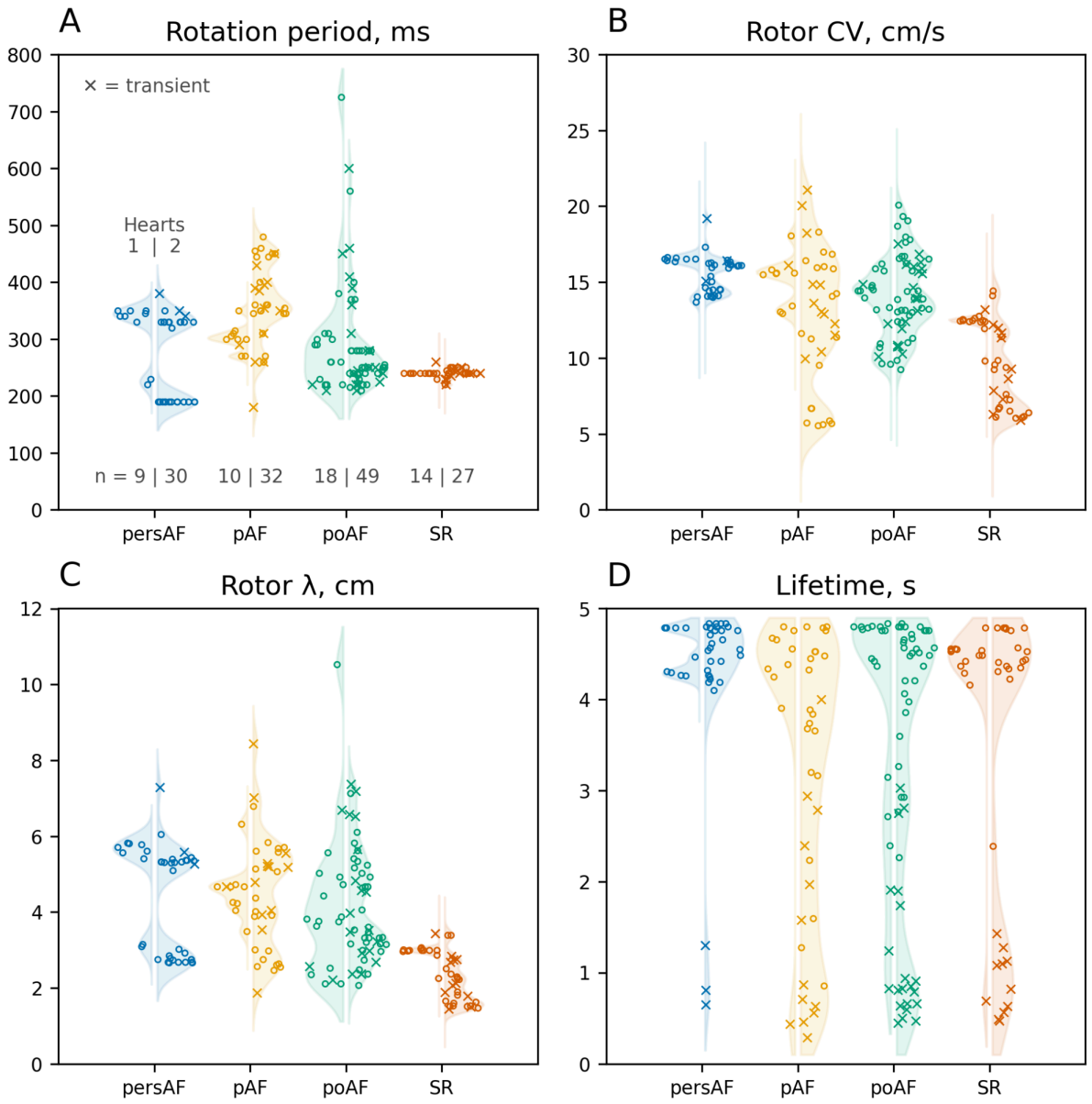

Figure S8. Reentrant drivers characteristics.
Rotation period (A), conduction velocity (B), wavelength (C), and lifetime (D). 'x' marks transient RDs, *i.e.* it self-terminates before the end of the simulation. Multimodality is caused by reentrant drivers located in different anatomical regions. For example, the high CL mode of the persAF group corresponds to RDs around pulmonary veins (anatomical block)

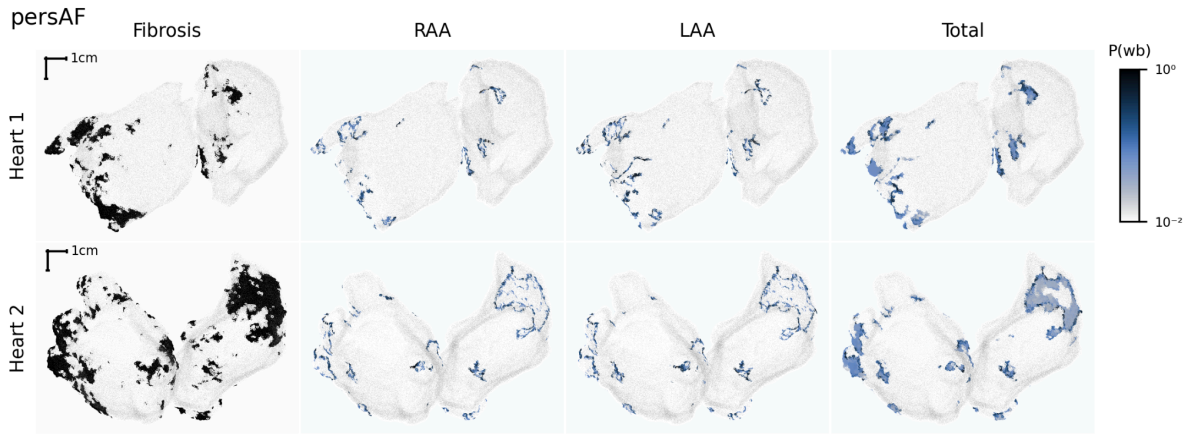

Figure S9. Wavebreak probability, P(wb), is independent of the pacing site. The first column is the fibrosis distribution (white and black are normal and fibrotic regions, respectively). The second and third columns correspond to the two simulations where stimuli were delivered to RAA and LAA, respectively. The last column shows the P(wb) averaged over all 40 simulations (pacing sites). The spatial distribution of the P(wb) depends on the fibrosis distribution and is very similar across different simulations.

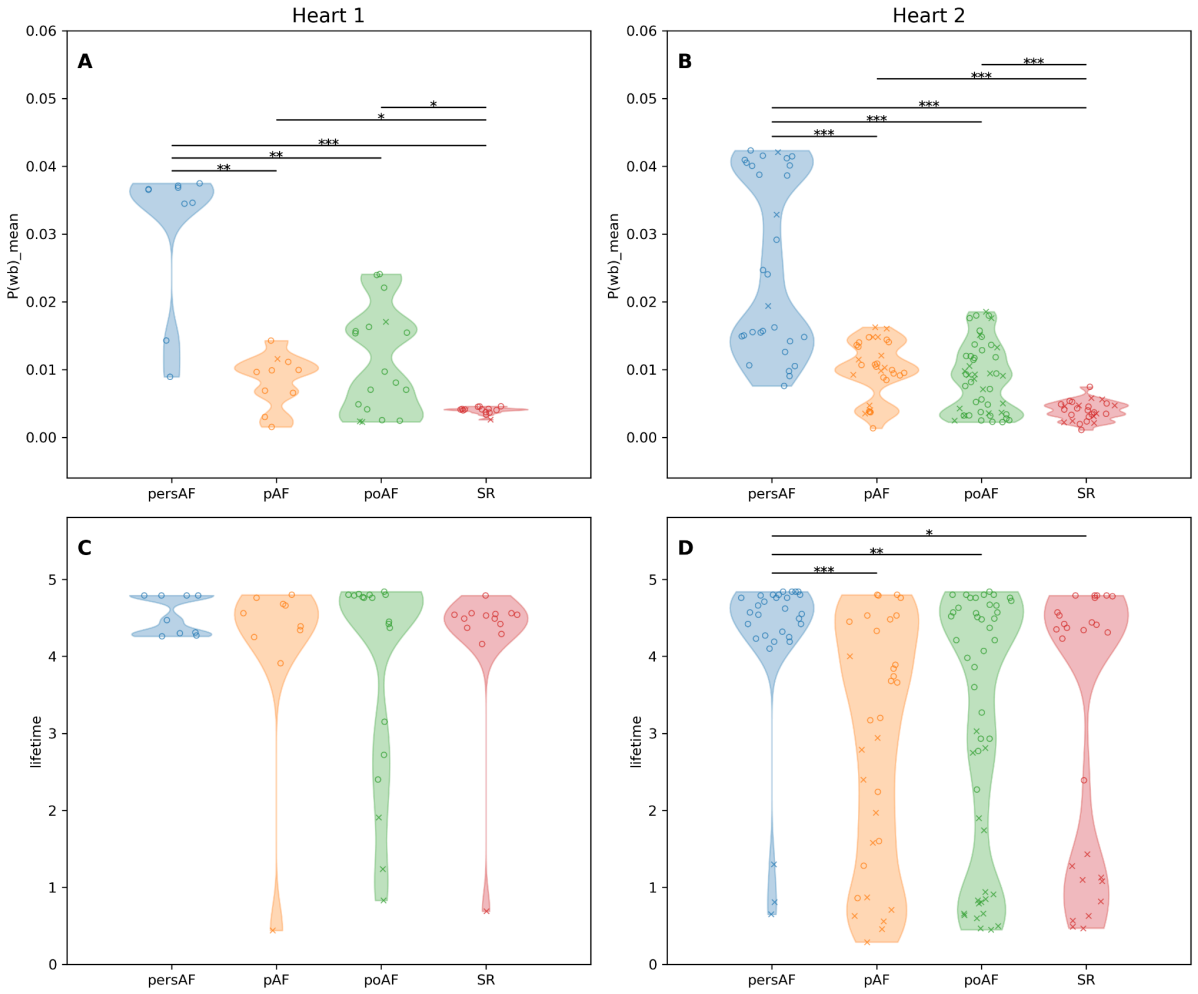

Figure S10. Wavebreak probability, P(wb), and RD lifetime comparison between AP models within the same geometry.

(A, C) show mean wavebreak probabilities (P(wb)) within RDs and RD lifetimes in Heart 1; (B, D) show the same for Heart 2. P(wb) differed significantly across all AP models except between pAF and poAF. RDs were more stable in the persAF model, resulting in significantly longer lifetimes in Heart 2. In Heart 1, the difference was not significant due to fewer transient RDs. Significance was assessed using two-sided Mann–Whitney test ($p < 0.05$*, *$p < 0.01$, **$p < 0.001$).